Constitutive analysis of hot metal flow behavior of virgin and rejuvenated heat treatment creep exhausted power plant X20 steel

Shem Elahetia Maube (smaube@gmail.com)
Dedan Kimathi University of Technology
Japheth Oirere Obiko
Josias Van der Merwe
Fred Mwema Madaraka
Desmond Klenam
Michael Oluwatosin Bodunrin

Research Article

Keywords: X20, Rejuvenation, Hot Deformation, Heat Treatment, Constitutive Analysis

Posted Date: November 10th, 2023

DOI: https://doi.org/10.21203/rs.3.rs-3564944/v1

Abstract

This paper presents constitutive equations that describe the hot flow behaviour of Virgin (VG) X20 and rejuvenated heat-treated creep exhaust (CE) X20 steels. The study provides a foundation for determining the effect of rejuvenation heat treatment on CE steels by making comparisons to the VG steel. Hot compression tests in the temperature range of 900°C to 1050°C, strain rate range of 0.1–10 s^{-1} to a total strain of 0.6 and stress-strain curves were obtained. The flow stress curves of both steels exhibited dynamic recovery (DRV) characteristics as the main softening mechanism. Constitutive constants of steady-state stresses were determined. The stress exponents, n, were 6.62 (VG) and 5.58 (CE), and the apparent activation energy values were 380.36 $kJmol^{-1}$(VG) and 435.70 $kJmol^{-1}$ (CE). Analysis of the activation energies showed that VG steel had better workability properties than CE steel and was easier to deform at high temperatures. Constitutive equations for predicting the flow stress in the two steels were established. This were verified by statistical tools: Pearson's correlation coefficient (R) and Absolute Average Relative Error (AARE). The results showed R-values were, 0.98 (VG) and 0.99 (CE), and the AARE value for VG was 4.17% and 9.01% for CE. The statistical parameters indicated a good correlation between the experimental and predicted values. The constitutive equations therefore adequately described the flow stress behaviour of both steels and can therefore efficiently analyse industrial metal forming schedules.

Introduction

Martensitic-ferritic 9–12% Cr steels are widely used for creep-resistant components operating at elevated temperatures in steam power-generating plants [1]. One of the 9–12% Cr steels, that operate at the creep range in thermal and steam power generation is the X20 CrMoV12-1 steel (hereby referred to as X20). X20 has been extensively used since the 1960s for tubes and pipework of thermal power plants operating at temperatures of up to 565°C [2]. This steel exhibits high creep strength, excellent corrosion, and fatigue resistance [4–7].

The Creep strength of X20 steel is obtained from solid solution hardening and precipitation strengthening. Before service, the steel components undergo a heat treatment procedure of austenitisation followed by air cooling, and tempering [8]. After heat treatment, the microstructure of the X20 steel is tempered martensite with precipitates along grain boundaries [10, 11]. Some of the precipitates are the carbides of the precipitates, such as $M_{23}C_6$, M_7C_3, M_2X, and MX [2]. In the X20CrMoV12-1 steel, $M_{23}C_6$ carbides (M = Cr, Mo) produce the main creep-strengthening mechanisms by precipitating along the sub-grain interior while MX (M = V, N) carbonitrides precipitate in the matrix enhancing high-temperature stability during service [11]. Further strengthening is provided by grain refinement from the formation of the tempered martensite structure with high dislocation density and high Cr and Mo providing solid solution strengthening [12].

Long-term exposure of the X20 steam pipes in thermal plants at creep temperatures causes changes to the microstructure and carbide morphology resulting in material exhaustion [13]. The changes induced

during service include, softening of the martensite matrix, change in the precipitation composition, the disappearance of prior austenite grain boundaries (PAGB), formation of sub-grains, and emergence of undesirable secondary phases, such as the Z phase [9, 15, 16]. The Z-phase (Cr (V, Nb) N) is similar in chemical elements to MX (Metal: V, Nb, and X: N) precipitates, with the only difference being chromium [16].

During service, the MX particles transform into the more stable and relatively coarse Z-phase [17]. This causes large spacing between particles hence lower creep strength [14]. The presence of higher chromium content in X20 steel (up to 12% Cr) further accelerates the precipitation of the Z-phase, causing microstructural degradation [11]. The evolution of microstructure during service therefore causes degradation of mechanical properties and shorter operational periods.

After a failure or end of design life, the X20 pipes are decommissioned and scraped. The high costs involved in the replacement of pipes have generated an increased industrial interest in prolonging the operational life of the exhaust steel [18]. Researchers have suggested the rejuvenation heat treatment process for restoring the properties and microstructure of creep-exhausted metals and alloys to their original condition [5, 19–21]. In this case, a two-stage heat treatment process: normalisation and tempering (N + T), has been suggested by researchers [9, 22]. During the normalisation process, the dissolution of microstructural phases occurs, forming a single-phase microstructure [22]. After tempering, the desired microstructure is achieved thus enhancing solid solution strengthening [15]. Previous studies on 12 wt.% Cr steels have focused on the effects of rejuvenation heat treatment on mechanical properties and microstructure evolution of aged power plant steels [7, 22, 23]. However, the literature on metal flow behaviour and constitutive modelling of rejuvenated heat-treated creep-exhausted steels X20 steel is conspicuously missing in the literature. In this study rejuvenation heat treatment procedure of normalising and tempering was applied to 100,000hr (CE) X20 steel. Hot compression testing was conducted using a Gleeble® 3500 thermal-mechanical simulator on the CE steel and VG steel, which was the control sample under the same conditions. Constitutive equations were then developed to explore the hot flow behaviour of the two steels and evaluate their suitability to predict flow stress through statistical methods.

Experimental procedure

In this study, the experimental materials used were virgin and creep-exhausted X20 steels for steam pipes. Table 1 shows the chemical composition (wt%) of the steels. All the samples were cut to a height of 12 mm and a diameter of 8 mm. The creep-exhausted samples were subjected to heat treatment rejuvenation procedures: normalisation at 1050°C for 40 minutes, air-cooled, tempered at 760°C for 120 minutes, followed by air cooling.

Table 1
Chemical composition of X20 the steels.

Elements	Mn	C	Cr	P	Ni	Mo	V	Cu	W	Nb
(wt.%)	0.46	0.198	11.35	0.02	0.648	0.909	0.259	0.086	0.01	0.76

The hot compression tests were carried out using a Gleeble®3500 thermo-mechanical simulator following a schedule shown in Fig. 1. The compression tests were conducted at temperatures of 900°C to 1050°C at intervals of 50°C and strain rates of 0.1 s^{-1}, 1 $s^{-1,}$ and 10 s^{-1} to a total strain of 0.6. The interface between the anvil and workpiece had graphite foil with nickel paste to reduce friction. The flow stress-strain curve data obtained from the experiment were recorded automatically by the Gleeble simulation software. The effect of friction reduction during deformation is not entirely possible. The stress-strain curves therefore were corrected for friction using an analytical equation [23] for barrelling coefficient (b) ≥ 1.1 [24].

Results and Discussion

3.1 Flow stress-strain curves

Figure 2 and Fig. 3 are the flow stress-strain curves obtained from hot compression testing for all conditions of deformation for the VG and CE steels. As seen, both steels exhibit similar flow stress behaviour and are sensitive to the deformation temperature and strain rate. At a constant strain rate, the flow stresses decrease with an increase in the temperature of deformation. This is attributed to the increase in deformation temperature which causes an increase in the rate of vacancy diffusion, climb of edge dislocations, and cross-slip of screw dislocations [26–28]. In the early stages (at strains < 0.2), work hardening prevails the deformation mechanisms causing a rapid increase in the dislocation density. The high dislocation density resists the deformation process, causing an increase in the flow stress. As the deformation progresses (to strains > 0.2), the flow stress curves display limited work hardening due to the increased softening effect. The decrease in flow stress progresses until the effect of work hardening and dynamic softening reaches an equilibrium. At this stage, the flow stress curves show steady-state flow stress where there is a relatively constant dislocation density. This characteristic flow behaviour suggests that DRV is the main softening mechanism [28].

Figure 2 Flow stress-strain curves for VG steel at different strain rates and temperatures

At constant temperature, the flow stress increases as the strain rate increases. Deformation at a higher strain rate causes a higher rate of dislocation multiplication, resulting in the dislocation-strengthening effect. This phenomenon causes higher resistance to deformation due to work hardening, which controls the deformation process at a high strain rate. This, therefore, causes deformation difficulties resulting in higher flow stresses [29]. During deformation at low strain rates, there is more time for dynamic recovery to occur, hence weakening the effect of work hardening. This relationship is observed in both steels at all temperatures and illustrated by Fig. 2d) for VG and Fig. 3d) at 1050°C.

Flow stress-strain curves reflect the effect of deformation conditions on the microstructure. Microstructural changes are related closely to the deformation mechanisms controlling the metal flow behaviour during hot forming [30]. Work hardening (WH) and flow softening mechanisms, such as dynamic recrystallization (DRX) and DRV, are reliant on the parameters during forming. The main flow softening mechanism of creep-resistant steels such as X20 with high stacking fault energy is DRV. During deformation, these steels easily re-arrange into polygonal sub-grain structures by dislocation climb and cross-slip, resulting in DRV[31]. The flow stress curves in Fig. 2 for VG and Fig. 3 for CE exhibited similar flow behaviour. It was observed that at strains below 0.2, WH dominated the deformation, and above 0.2, the curves exhibited DRV softening mechanisms until the end of the deformation process. This result implies that the hot working of the rejuvenated heat treatment CE steels within the temperature range of 950–1100°C, would allow the recycling of the steel by hot deformation into new components with comparable flow characteristics of the virgin steel.

3.2 Flow stress curve modelling

3.2.1. Constitutive modelling

Constitutive equations are applied widely in the analysis of metal flow behaviour for various metals and alloys during deformation [33–36]. These equations form a basis for developing models that are used to predict flow stress behaviour at all deformation conditions [36]. For example, the Arrhenius equation is widely applied to describe the relationship between flow stress (σ), strain rate (ἐ), and temperature (T) [38–41].

$$\dot{\epsilon} = \mathrm{A}\mathrm{f}(\sigma)\exp\left(\frac{-\mathrm{Q}}{\mathrm{RT}}\right)$$

(1)

$$\mathrm{f}(\sigma) = \left\{ \begin{array}{c} A\sigma^{\mathrm{n}'} for low flow stress \alpha\sigma < 0.8 \\ \mathrm{A}\exp\left(\beta'\sigma\right) for high flow stress \alpha\sigma > 1.2 \\ A[\sinh(\alpha\sigma)]^{\mathrm{n}} for all stress \sigma \end{array} \right\}$$

(2)

From Equations (1) and (2), Q is the activation energy for deformation in kJ/mol, and R is the universal gas constant [8.3145 J/(mol. K)]. A, β, n', σ, and n are material constants. α is the stress multiplier. The constitutive constants and activation energy are derived using the general case of the Arrhenius equation [40]. Substituting f (σ) values into Equations (1) and taking natural logarithms on either side gives:

$$\ln\dot{\epsilon} = \ln\mathrm{A} - \frac{\mathrm{Q}}{\mathrm{RT}} + \mathrm{n}'\ln\sigma$$

(3)

$$\ln\dot{\epsilon} = \ln A - \frac{Q}{RT} + \beta\sigma$$

(4)

$$\ln\dot{\epsilon} = \ln A - \frac{Q}{RT} + n\ln Sinh\,(\alpha\sigma)$$

(5)

Material constants were obtained using the saturation stress (Q_{sat}) in the Arrhenius type equation [41]. The saturation flow stresses were obtained directly from the stress vs strain curves at the steady-state flow stress value [34, 44]. The values of n' and β were obtained from slopes of plots of (ln (ἐ) against ln σ), and (ln (ἐ) against σ) as presented in Fig. 4a) – b) (VG) and Fig. 5a) – b) (CE). The stress multiplier is obtained from α = β / n [43]. n (∂ ln ἐ against ∂ ln (sinh (ασ)) and S (∂ ln (sinh (ασ) against ∂ (1/T)) are obtained from average slope values of graphical plots of ln ἐ against ln (sinh (ασ)) and 1000/T against ln (sinh (ασ)), as shown in Fig. 4 (c - d) for VG and Fig. 5 (c - d) for CE. By differentiating Equation (5), the activation energy is obtained as follows [44]:

$$Q = RnS = R\left[\frac{\partial \ln\dot{\epsilon}}{\partial \ln[\sinh(\alpha\sigma)]}\right]_T \left[\frac{\partial \ln[\sinh(\sigma\sigma)]}{\partial(\raisebox{1ex}{\$1\$}\!\!\raisebox{-1ex}{\$T\$})}\right]_\epsilon \quad 6$$

3.2.2. Zener-Hollomon parameter analysis

The effects of strain rate and temperature on hot deformation behaviour relate well with Zener -Hollomon parameter Z [41, 45]. This parameter characterises the influence of deformation conditions (strain rate and temperature) on the workability of the metals and alloys. The Z-parameter is as Equation (7) [46].

$$Z = \dot{\epsilon}\exp\left(\frac{Q}{RT}\right) = A[Sinh\,(\alpha\sigma)]^n \quad (7)$$

Taking logarithms on either side of Equation (7), the equation may be written as follows.

$$\ln Z = \ln A + n\ln[\sinh(\alpha\sigma)] \quad (8)$$

By substituting values of Q into Equation (7), the value of Z can be obtained. The linear relationship between ln Z against ln [sinh (αα)] is shown in Fig. 6a) for VG and b) for CE. The correlation index, R2 for VG (0.98) and CE (0.99) shows a highly linear relationship between ln Z and ln [sinh (ασ)] in both steels. The high R2 values for the test conditions suggested that a single deformation mechanism controlled the process. ln A was obtained as the intercept of the plot of ln Z vs ln [sinh (αα)]. Table 2 is a summary of constitutive constants and activation energies of the VG and CE steels.

Table 2
Constitutive constants and activation energy for VG and CE steels.

X20 Steel	$\acute{H}$	β	η	a (MPa^{-1})	S	Q ($kJmol^{-1}$)	A
VG	8.843	0.045	6.62	0.005	6.910	380.36	5.099×10^{15}
CE	7.787	0.046	5.79	0.006	9.047	435.70	2.977×10^{17}

3.2.3. Material constants for VG and CE steels

Table 2. shows the constitutive constants derived from modelled equations for the VG and CE steels. The stress exponent, n, and activation energy for hot working, Q are important parameters as they provide information on plastic deformation and underlying mechanisms controlling the process. The stress exponents of the two steels were analysed and the stress exponents obtained were VG (6.6), and CE (5.8). Studies by various authors [46, 50] have shown that a stress exponent value below 5 indicates the occurrence of DRX during hot deformation. Other reports [49–51] have established that when the stress exponent is 5, the deformation process is controlled by the climb and glide dislocation mechanisms. Studies by Mirzadeh et al. [40] have suggested that in flow stress curves exhibiting DRV softening, dislocation climb and glide are the main controlling mechanisms. It is observed in Fig. 2 for VG and Fig. 3 for CE that the flow stress curves exhibit typical DRV flow softening behaviour. There are no peaks displayed followed by steady-state flow stress that is associated with DRX. It was therefore determined that the main deformation mechanism in the two steels was dislocation glide controlled by dislocation climb. A comparison of the stress exponents for the two steels showed a slight variation between the values for the VG and CE steels. The variation in the stress exponent values can be attributed to the differences in precipitation evolution during deformation for the two steels. Generally, the presence of carbides impedes motion of dislocations causing an increase in the stress exponent value [30]. Deformation at higher temperatures causes increased carbide dissolution hence, deformation occurring at the austenitic field may result in lower stress exponent values [49].

Apart from the stress exponent, the apparent activation energy for hot working is an indicator of mechanisms that control the deformation process. The activation energy obtained using Arrhenius equations does not represent the microstructural changes occurring during deformation [50]. It is therefore called ‘apparent activation energy’ as the equations assume the microstructure remains constant during deformation [50, 51]. The apparent activation energies obtained in this study were VG (380.36 $kJmol^{-1}$) and CE (435.7 $kJmol^{-1}$). These values differ greatly from the self-diffusion activation energy (Q_{SD}) of iron in austenite (270 $kJmol^{-1}$) and for α-Fe in ferrite (250 $kJ.mol^{-1}$) [30].

Wang et al. [53] described the deviation of activation energy from the imagined atomic mechanisms in terms of variation of temperature with Young’s modulus [51]. McQueen and Ryan [54] explained that during hot working, the initial microstructure differs to some degree for different preheats and evolves quickly when testing. Other researchers have suggested that micro-alloying elements such as Cr and Mo play an important role as they increase the activation energy by solute drag effect and solid solution

strengthening mechanisms [30, 53]. Further, the presence of precipitates, solutes, dispersoids, reinforcements, and inclusions also increases the activation energy by 50% [54].

As stated earlier, the activation energy is an indicator of the workability properties of a material during forming. It defines the level of resistance or difficulty to deformation a material poses to a hot working process. Comparisons of the activation energies of the two steels show, that VG steel was lower than CE. From the hot workability viewpoint, it suggests that VG steel had better workability compared to CE steel. The variation in activation energy between VG and CE may be ascribed to the variation in phase compositions during the deformation of the two steels.

The Phase compositions and precipitates influence the deformation process and therefore material constants. During hot deformation, material constants vary significantly with process parameters and the deformation temperature. The deformation temperature, in turn, influences the evolutions in microstructure and the resulting material flow stress. Flow stress directly affects the activation energy during hot deformation as flow stress increases with the activation energy for deformation [30].

The results of the apparent activation energies for the two steels indicate the energy required for initiating and maintaining the motion of dislocations within the crystals of the rejuvenation heat treatment CE steel was higher than that of the VG steel. It is concluded that the rejuvenation effect increased the materials' hot deformation resistance compared to that of the VG steel. The heat treatment CE steel would therefore have suitable application as recycled steel in an environment where resistance to plastic deformation at elevated temperatures would be desirable.

3.2.4 Constitutive models of the flow stresses

Using the saturated stresses obtained from stress-strain curves in the hyperbolic sine law; constitutive equations for the two steels are given as follows:

VG $\dot{\epsilon} = 5.0999 \times 10^{15}[\sinh(0.00503\sigma_{ss})]^{6.62}\exp\left[\frac{-380.361}{RT}\right]$ (9)

CE $\dot{\epsilon} = 2.9774 \times 10^{17}[\sinh(0.00601\sigma_{ss})]^{5.79}\exp\left[\frac{-435.699}{RT}\right]$ (10)

The material constants derived using the Arrhenius equations (Section 3.2.1) can model flow behaviour for the two steels using the Z parameter. From Equation (7), the solution of this equation gives Equation (11) [46] as:

$$\sigma = \frac{1}{\alpha}\ln\left\{\left(\frac{Z}{A}\right)^{1/n} + \left[\left(\frac{Z}{A}\right)^{2/n} + 1\right]^{1/2}\right\} \quad (11)$$

From Equation (11) the saturation flow stresses of VG and CE can be determined as follows:

$$\text{VG } \sigma = \frac{1}{0.005}\ln\left\{\left(\frac{Z}{5.099\times10^{15}}\right)^{\frac{1}{6.62}} + \left[\left(\frac{Z}{5.099\times10^{15}}\right)^{\frac{2}{6.62}} + 1\right]^{1/2}\right\} \quad (12)$$

$$\text{CE } \sigma = \frac{1}{0.006}\ln\left\{\left(\frac{Z}{2.977\times10^{17}}\right)^{\frac{1}{5.79}} + \left[\left(\frac{Z}{2.977\times10^{17}}\right)^{\frac{2}{5.79}} + 1\right]^{1/2}\right\} \quad (13)$$

3.2.5. Model validation

Verification of Equations (12) and (13) for the two steels (VG and CE) was done by comparison of flow stresses of the experimental and predicted data. The standard statistical parameters used to analyse the predictability of the equations were Pearson's correlation coefficient (Equation(14)) and Average Absolute Relative Error (AARE) (Equation(15)). Figure 7 ((a) and (b)) are plots of the experimental against predicted flow stresses obtained using Equations (12) and (13). The plots had a good correlation coefficient of 0.98 for the VG steel and 0.99 for the CE steel, where a value of 1.00 is a perfect correlation. The correlation coefficient method is however liable to bias towards high or low values therefore affecting the models' accuracy. The AARE statistical analysis method complements Pearson's correlation coefficient as it gives good accuracy and quantifies prediction deviation. In the AARE method, the calculation is through a term-by-term comparison of the relative error in the analysis of the developed equations. A lower AARE value signifies a higher accuracy of the constitutive model to predict the flow stresses and vice versa. The AARE values obtained were: VG (4.17%) and CE (9.01%). The AARE for VG indicated excellent predictability of the constitutive equation than CE. From the calculated parameters, the Arrhenius constitutive equation developed for the two steel has a high prediction accuracy of flow stress for all test conditions.

$$R = \frac{\sum_{i=1}^{N}(P_i - P)(E_i - E)}{\sqrt{\sum_{i=1}^{N}(P_i - P)^2}\sqrt{\sum_{i=1}^{N}(E_i - E)^2}} \quad (14)$$

$$AARE = \frac{1}{N}\sum_{i=1}^{N}\left|\frac{E_i - P_i}{E_i}\right| \times 100\% \quad (15)$$

Where E_i is the experimental flow stress, Pi is the predicted flow stress obtained from constitutive equations, E and P, are mean flow stress values of experimental data E, P is the predicted data, and N is sum of the data points.

Conclusions

Hot deformation tests were studied for (VG) and heat-treated creep exhaust steel (CE) for a wide range of deformation conditions using a Gleeble® 3500 thermo-mechanical simulator. The outcomes of the

investigation are as below:

1. The flow stress-strain curves of the CE steel, exhibited similar flow behaviour to the VG steel. In the initial deformation stages (strains 0.2), work hardening (WH) controlled the deformation mechanisms for the two steels. At higher strains (> 0.2), the slopes of the flow stress curves reduced until the flow stress reached a steady-state flow stress owing to the flow-softening effect of DRV.
2. The stress exponent, n, for VG, was 6.62, and the CE steel was 5.79. The apparent activation energy, Q of VG steel was 380.36 kJ/mol, and for the rejuvenation, heat treatment CE steel was 435.70 kJ/mol. The rejuvenation effect on the apparent activation energy on the CE steel showed the steel to be harder to deform than the VG steel at elevated temperatures. This indicates that rejuvenation heat treatment can be used to restore creep exhaust X20 steel for reuse in thermal power plant components.
3. Two constitutive equations were developed for the two steels at a true strain of 0.6 as follows:

   i. For VG steel:$\dot{\epsilon} = 5.0999 \times 10^{15}[\sinh(0.00503\sigma_{ss})]^{6.62}\exp\left[\frac{-380.36}{RT}\right]$

   ii; For CE steel :$\dot{\epsilon} = 2.9774 \times 10^{17}[\sinh(0.00601\sigma_{ss})]^{5.79}\exp\left[\frac{-435.70}{RT}\right]$

   4. The developed constitutive models were validated using standard statistical parameters: Pearson's correlation coefficient (R) and the Average Absolute Relative Error (AARE). The R obtained for VG was 0.99, and AARE was 4.17%. For CE steel, R was 0.996, and AARE was 9.01%. The results established there was a good correlation between the experiment and predicted data.

Declarations

Funding

The authors declare that no funds, grants, or other support were received during the preparation of this manuscript.

Competing interest

The authors have no relevant financial or non-financial interests to disclose.

Author contributions

All authors contributed to the conceptualisation and design. Methodology and investigations were performed by Shem Maube, Japheth Obiko, Josias Van der Merwe, Fredrick Mwema, Desmond Klenam and Michael Bodunrin. The first draft of the manuscript was written by Shem Maube and all authors commented on previous versions of the manuscript. All authors read and approved the final manuscript.

References

1. D. A. Skobir, M. Godec, M. Jenko, and B. Markoli, “Characterization of the carbides in the steel X20CrMoV12.1 used in thermal power plants,” Surf. Interface Anal., vol. 40, no. 3–4, pp. 513–517, 2008, doi: 10.1002/sia.2759.
2. C. Pandey, M. M. Mahapatra, P. Kumar, and N. Saini, “Some studies on P91 steel and their weldments,” J. Alloys Compd., vol. 743, pp. 332–364, 2018, doi: 10.1016/j.jallcom.2018.01.120.
3. J. A. Francis, W. Mazur, and H. K. D. H. Bhadeshia, “Type IV cracking in ferritic power plant steels,” Mater. Sci. Technol., vol. 22, no. 12, pp. 1387–1395, 2006, doi: 10.1179/174328406X148778.
4. G. Bakic, V. Zeravcic, M. B. Djukic, and N. Perunicic, “Material Characterization of the Main Steam Gate Valve Made of X20CrMoV 12.1 Steel after Long Term Service,” Procedia Mater. Sci., vol. 3, pp. 1512–1517, 2014, doi: 10.1016/j.mspro.2014.06.244.
5. J. Hald, “Microstructure and long-term creep properties of 9-12% Cr steels,” Int. J. Press. Vessel. Pip., vol. 85, no. 1–2, pp. 30–37, 2008, doi: 10.1016/j.ijpvp.2007.06.010.
6. J. Brózda and M. Zeman, “Wrong heat treatment of martensitic steel welded tubes caused major cracking during assembly of resuperheaters in a fossil fuel power plant,” Eng. Fail. Anal., vol. 10, no. 5, pp. 569–579, 2003, doi: 10.1016/S1350-6307(03)00039-6.
7. S. Salifu, D. Desai, and S. Kok, “Numerical simulation and creep-life prediction of X20 steam piping,” Mater. Today Proc., vol. 38, no. xxxx, pp. 893–898, 2021, doi: 10.1016/j.matpr.2020.05.125.
8. D. R. Barraclough and D. J. Gooch, “Effect of inadequate heat treatment on creep strength of 12Cr–Mo–V steel,” Mater. Sci. Technol. (United Kingdom), vol. 1, no. 11, pp. 961–967, 1985, doi: 10.1179/mst.1985.1.11.961.
9. J. Hald, “Metallurgy and creep properties of new 9-12%Cr steels,” Steel Res., vol. 67, no. 9, pp. 369–374, 1996, doi: 10.1002/srin.199605503.
10. H. K. Danielsen and J. Hald, “Behaviour of z phase in 9–12%Cr steels,” Energy Mater. Mater. Sci. Eng. Energy Syst., vol. 1, no. 1, pp. 49–57, 2006, doi: 10.1179/174892306X99732.
11. H. K. Danielsen, “Review of Z phase precipitation in 9-12 wt-%Cr steels,” Mater. Sci. Technol. (United Kingdom), vol. 32, no. 2, pp. 126–137, 2016, doi: 10.1179/1743284715Y.0000000066.
12. G. Bakic, V. Zeravcic, M. B. Djukic, and N. Perunicic, “Material Characterization of the Main Steam Gate Valve Made of X20CrMoV 12.1 Steel after Long Term Service,” Procedia Mater. Sci., vol. 3, pp. 1512–1517, 2014, doi: 10.1016/j.mspro.2014.06.244.
13. Z. F. Hu and Z. G. Yang, “Identification of the precipitates by TEM and EDS in X20CrMoV12.1 after long-term service at elevated temperature,” J. Mater. Eng. Perform., vol. 12, no. 1, pp. 106–111, 2003, doi: 10.1361/105994903770343556.
14. L. Cipolla, H. K. Danielsen, P. E. Di Nunzio, D. Venditti, J. Hald, and M. A. J. Somers, “On the role of Nb in Z-phase formation in a 12% Cr steel,” Scr. Mater., vol. 63, no. 3, pp. 324–327, 2010, doi: 10.1016/j.scriptamat.2010.04.025.

15. W. Yan, W. Wang, Y. Y. Shan, and K. Yang, “Microstructural stability of 9-12%Cr ferrite/martensite heat-resistant steels,” Front. Mater. Sci., vol. 7, no. 1, pp. 1–27, 2013, doi: 10.1007/s11706-013-0189-5.
16. H. K. Danielsen and J. Hald, “On the nucleation and dissolution process of Z-phase Cr(V,Nb)N in martensitic 12%Cr steels,” Mater. Sci. Eng. A, vol. 505, no. 1–2, pp. 169–177, 2009, doi: 10.1016/j.msea.2008.11.019.
17. L. Cipolla, H. K. Danielsen, D. Venditti, P. E. Di Nunzio, J. Hald, and M. A. J. Somers, “Conversion of MX nitrides to Z-phase in a martensitic 12% Cr steel,” Acta Mater., vol. 58, no. 2, pp. 669–679, 2010, doi: 10.1016/j.actamat.2009.09.045.
18. A. Baldan, “Rejuvenation procedures to recover creep properties of nickel-base superalloys by heat treatment and hot isostatic pressing techniques - A review,” Journal of Materials Science, vol. 26, no. 13. pp. 3409–3421, 1991, doi: 10.1007/BF00557126.
19. S. Lin, H. Shen, G. Zhou, W. He, and K. Chen, “A new rejuvenation heat treatment of crept Ni-based superalloy single crystals,” IOP Conf. Ser. Mater. Sci. Eng., vol. 1249, no. 1, p. 012017, 2022, doi: 10.1088/1757-899x/1249/1/012017.
20. L. Falat, L. Čiripová, V. Homolová, M. Džupon, R. Džunda, and K. Koval’, “The effects of various conditions of short-term rejuvenation heat treatment on room-temperature mechanical properties of thermally aged P92 boiler steel,” Materials (Basel)., vol. 14, no. 20, 2021, doi: 10.3390/ma14206076.
21. R. C. Thomson and H. K. D. H. Bhadeshia, “Carbide precipitation in 12Cr1MoV power plant steel,” Metall. Trans. A, vol. 23, no. 4, pp. 1171–1179, 1992, doi: 10.1007/BF02665048.
22. C. Pandey, M. M. Mahapatra, P. Kumar, and N. Saini, “Homogenization of P91 weldments using varying normalizing and tempering treatment,” Mater. Sci. Eng. A, vol. 710, no. June 2017, pp. 86–101, 2018, doi: 10.1016/j.msea.2017.10.086.
23. J. Obiko, “Friction correction of flow stress-strain curve in the upsetting process,” IOP SciNotes, vol. 2, no. 1, p. 014401, 2021, doi: 10.1088/2633-1357/abdd96.
24. J. Li et al., “Research on Hot Deformation Behavior of F92 Steel Based on Stress Correction,” Metals (Basel)., vol. 12, no. 5, pp. 1–14, 2022, doi: 10.3390/met12050698.
25. Y. V. R. K. Prasad and K. P. Rao, “Processing maps for hot deformation of rolled AZ31 magnesium alloy plate: Anisotropy of hot workability,” Mater. Sci. Eng. A, vol. 487, no. 1–2, pp. 316–327, 2008, doi: 10.1016/j.msea.2007.10.038.
26. Z. B. Xiao, Y. C. Huang, and Y. Liu, “Modeling of Flow Stress of 2026 Al Alloy under Hot Compression,” Adv. Mater. Sci. Eng., vol. 2016, pp. 28–32, 2016, doi: 10.1155/2016/3803472.
27. F. Ren, F. Chen, J. Chen, and X. Tang, “Hot deformation behavior and processing maps of AISI 420 martensitic stainless steel,” J. Manuf. Process., vol. 31, pp. 640–649, 2018, doi: 10.1016/j.jmapro.2017.12.015.
28. A. S. Taylor and P. D. Hodgson, “Dynamic behaviour of 304 stainless steel during high Z deformation,” Mater. Sci. Eng. A, vol. 528, no. 9, pp. 3310–3320, 2011, doi: 10.1016/j.msea.2010.12.093.

29. S. Ghosh, M. C. Somani, D. Setman, and S. Mula, “Hot Deformation Characteristic and Strain Dependent Constitutive Flow Stress Modelling of Ti + Nb Stabilized Interstitial Free Steel,” Met. Mater. Int., vol. 27, no. 8, pp. 2481–2498, 2021, doi: 10.1007/s12540-020-00827-1.
30. J. Obiko, L. Chown, D. Whitefield, and M. Bodunrin, “Metal flow behaviour and processing maps of high heat resistant steel during hot compression,” Int. J. Adv. Manuf. Technol., vol. 121, no. 5–6, pp. 4153–4167, 2022, doi: 10.1007/s00170-022-09577-3.
31. L. Wang, F. Liu, Q. Zuo, and C. F. Chen, “Prediction of flow stress for N08028 alloy under hot working conditions,” Mater. Des., vol. 47, pp. 737–745, 2013, doi: 10.1016/j.matdes.2012.12.074.
32. J. Obiko, L. Chown, D. Whitefield, and M. Bodunrin, “Understanding hot workability of power plant P92 creep resistant steels using dynamic material modelling (DMM) and microstructural evolution,” Int. J. Interact. Des. Manuf., 2022, doi: 10.1007/s12008-022-01084-9.
33. J. Obiko, L. H. Chown, and D. J. Whitefield, “Warm deformation behaviour of P92 steel,” Mater. Res. Express, vol. 6, no. 12, 2019, doi: 10.1088/2053-1591/ab5e9c.
34. G. Ge, L. Zhang, J. Xin, J. Lin, M. Aindow, and L. Zhang, “Constitutive modeling of high temperature flow behavior in a Ti-45Al-8Nb-2Cr-2Mn-0.2Y alloy,” Sci. Rep., vol. 8, no. 1, Dec. 2018, doi: 10.1038/s41598-018-23617-7.
35. H. Liu, Z. Cheng, W. Yu, G. Wang, J. Zhou, and Q. Cai, “Deformation behavior and constitutive equation of 42crmo steel at high temperature,” Metals (Basel)., vol. 11, no. 10, 2021, doi: 10.3390/met11101614.
36. Z. Cai, H. Ji, W. Pei, B. Wang, X. Huang, and Y. Li, “Constitutive equation and model validation for 33Cr23Ni8Mn3N heat-resistant steel during hot compression,” Results Phys., vol. 15, no. July, p. 102633, 2019, doi: 10.1016/j.rinp.2019.102633.
37. L. Jia, Y. Li, and Y. Zhang, “A Characterization for the Deformation Behavior of As-Cast P91 Alloy Steel and Utilization in Hot Extrusion Process,” Adv. Mater. Sci. Eng., vol. 2017, 2017, doi: 10.1155/2017/6582739.
38. N. Kumar, S. Kumar, S. K. Rajput, and S. K. Nath, “Modelling of flow stress and prediction of workability by processing map for hot compression of 43CrNi steel,” ISIJ Int., vol. 57, no. 3, pp. 497–505, 2017, doi: 10.2355/isijinternational.ISIJINT-2016-306.
39. N. Nayan et al., “Hot workability and microstructure control in Monel®400 (Ni–30Cu) alloy: An approach using processing map, constitutive equation and deformation modeling,” Mater. Sci. Eng. A, vol. 825, no. July, p. 141855, 2021, doi: 10.1016/j.msea.2021.141855.
40. H. Mirzadeh, J. M. Cabrera, and A. Najafizadeh, “Constitutive relationships for hot deformation of austenite,” Acta Mater., vol. 59, no. 16, pp. 6441–6448, 2011, doi: 10.1016/j.actamat.2011.07.008.
41. A. Laasraoui and J. J. Jonas, “Prediction of steel flow stresses at high temperatures and strain rates,” Metall. Trans. A, vol. 22, no. 7, pp. 1545–1558, 1991, doi: 10.1007/BF02667368.
42. A. Oudin, M. R. Barnett, and P. D. Hodgson, “Grain size effect on the warm deformation behaviour of a Ti-IF steel,” Mater. Sci. Eng. A, vol. 367, no. 1–2, pp. 282–294, 2004, doi: 10.1016/j.msea.2003.10.273.

43. K. K. Alaneme, S. A. Babalola, and M. O. Bodunrin, “On the prediction of hot deformation mechanisms and workability in Al6063/Nip and Al6063/steelp composites using hyperbolic-sine constitutive equation,” Mater. Today Proc., vol. 38, no. 10, pp. 942–948, 2021, doi: 10.1016/j.matpr.2020.05.463.
44. M. O. Bodunrin, “Flow stress prediction using hyperbolic-sine Arrhenius constants optimised by simple generalised reduced gradient refinement,” J. Mater. Res. Technol., vol. 9, no. 2, pp. 2376–2386, 2020, doi: 10.1016/j.jmrt.2019.12.070.
45. H. Wu, M. Liu, Y. Wang, Z. Huang, G. Tan, and L. Yang, “Experimental study and numerical simulation of dynamic recrystallization for a FGH96 superalloy during isothermal compression,” J. Mater. Res. Technol., vol. 9, no. 3, pp. 5090–5104, 2020, doi: 10.1016/j.jmrt.2020.03.026.
46. F. M. Mwema, J. O. Obiko, R. M. Mahamood, A. A. Adediran, M. O. Bodunrin, and E. T. Akinlabi, “Constitutive analysis of hot forming process of P91 steel: finite element method approach,” Adv. Mater. Process. Technol., vol. 00, no. 00, pp. 1–12, 2021, doi: 10.1080/2374068X.2021.1939560.
47. H. Mirzadeh, “Simple physically-based constitutive equations for hot deformation of 2024 and 7075 aluminum alloys,” Trans. Nonferrous Met. Soc. China (English Ed., vol. 25, no. 5, pp. 1614–1618, 2015, doi: 10.1016/S1003-6326(15)63765-7.
48. D. Q. Zhou, X. Q. Xu, H. H. Mao, Y. F. Yan, T. G. Nieh, and Z. P. Lu, “Plastic flow behaviour in an alumina-forming austenitic stainless steel at elevated temperatures,” Mater. Sci. Eng. A, vol. 594, pp. 246–252, 2014, doi: 10.1016/j.msea.2013.11.021.
49. M. Carsí, F. Peñalba, I. Rieiro, and O. A. Ruano, “High temperature workability behavior of a modified P92 steel,” Int. J. Mater. Res., vol. 102, no. 11, pp. 1378–1383, 2011, doi: 10.3139/146.110603.
50. M. El Wahabi, J. M. Cabrera, and J. M. Prado, “Hot working of two AISI 304 steels: A comparative study,” Mater. Sci. Eng. A, vol. 343, no. 1–2, pp. 116–125, 2003, doi: 10.1016/S0921-5093(02)00357-X.
51. R. Baktash and H. Mirzadeh, “A Simple Constitutive Model for Prediction of Single-Peak Flow Curves Under Hot Working Conditions,” J. Eng. Mater. Technol. Trans. ASME, vol. 138, no. 2, 2016, doi: 10.1115/1.4032153.
52. J. M. Cabrera, J. J. Jonas, and J. M. Prado, “Flow behaviour of medium carbon microalloyed steel under hot working conditions,” Mater. Sci. Technol., vol. 12, no. 7, pp. 579–585, 1996, doi: 10.1179/mst.1996.12.7.579.
53. S. Wang, J. R. Luo, L. G. Hou, J. S. Zhang, and L. Z. Zhuang, “Identification of the threshold stress and true activation energy for characterizing the deformation mechanisms during hot working,” Mater. Des., vol. 113, pp. 27–36, 2017, doi: 10.1016/j.matdes.2016.10.018.
54. H. J. McQueen and N. D. Ryan, “Constitutive analysis in hot working,” Mater. Sci. Eng. A, vol. 322, no. 1–2, pp. 43–63, 2002, doi: 10.1016/S0921-5093(01)01117-0.
55. Z. Yang, F. Zhang, C. Zheng, M. Zhang, B. Lv, and L. Qu, “Study on hot deformation behaviour and processing maps of low carbon bainitic steel,” Mater. Des., vol. 66, no. PA, pp. 258–266, 2015, doi: 10.1016/j.matdes.2014.10.068.

Figures

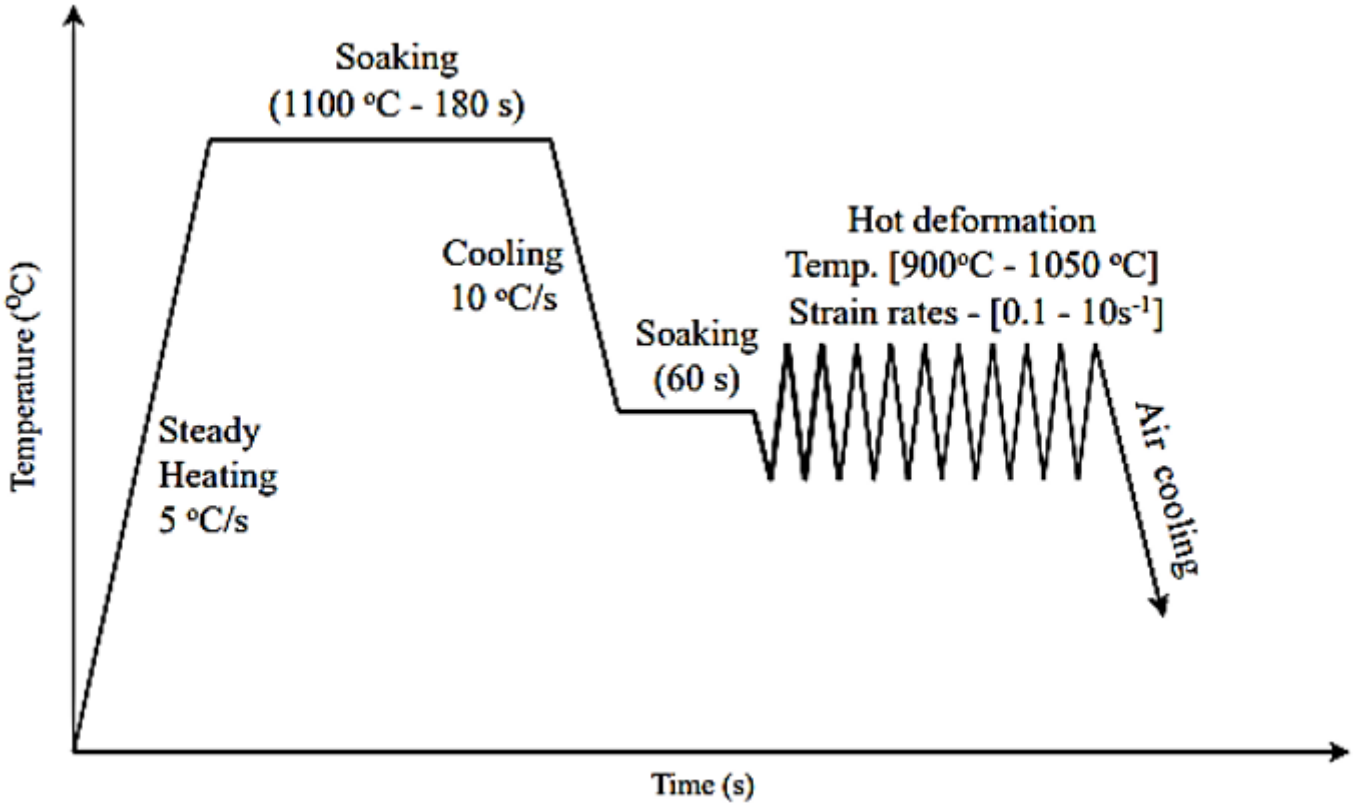

Figure 1

The thermal history of hot compression test

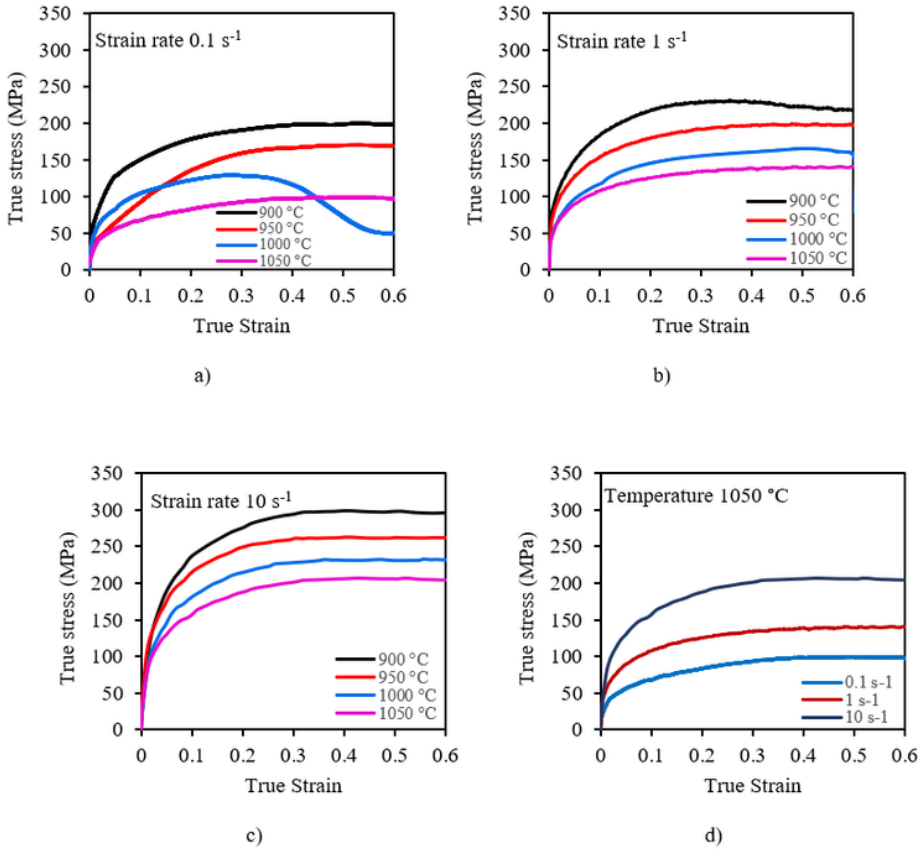

Figure 2

Flow stress-strain curves for VG steel at different strain rates and temperatures

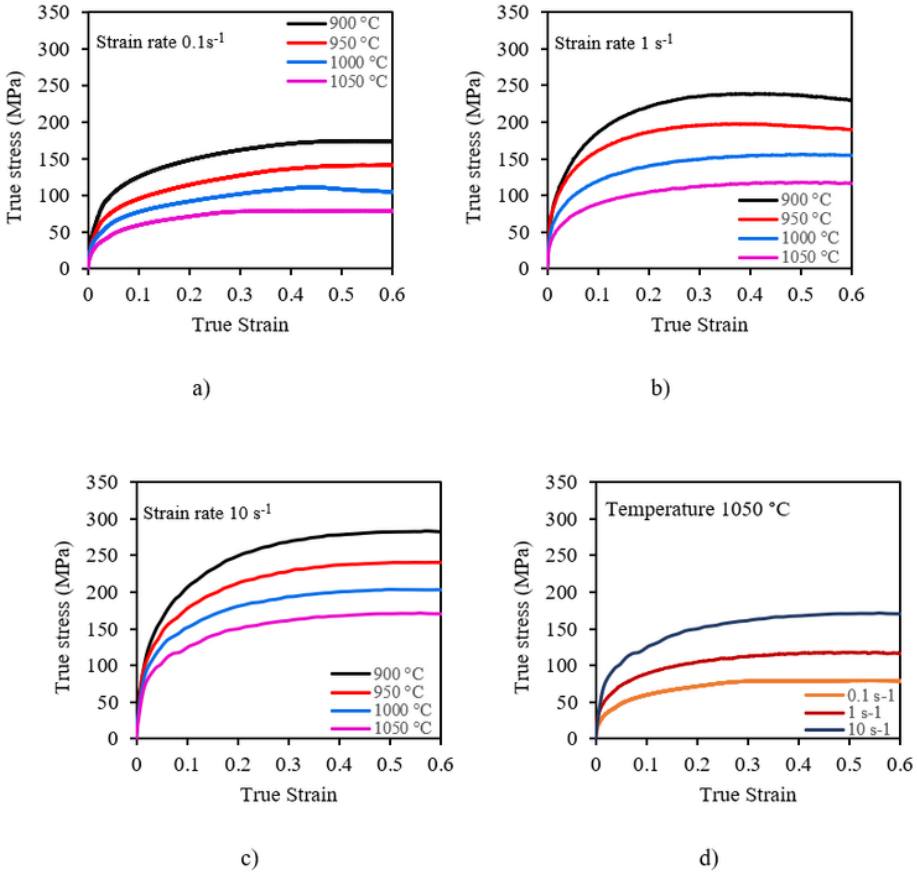

Figure 3

Flow stress–strain curves of CE steel at different strain rates and temperatures

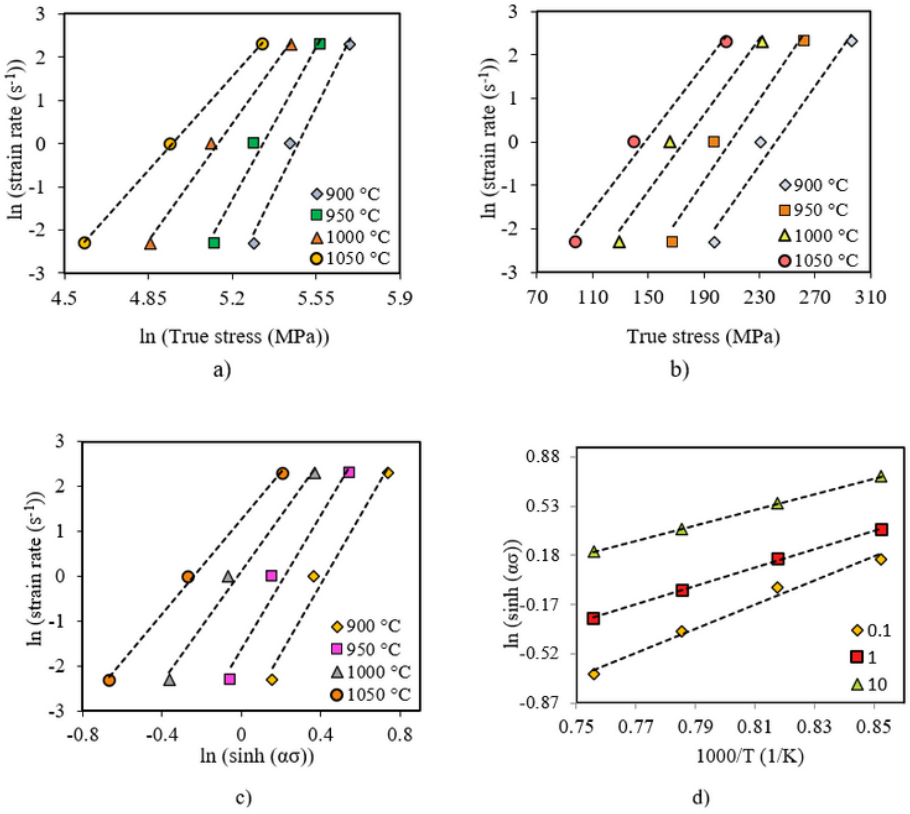

Fig. 4 Plots of a) ln ($\dot{\varepsilon}$) against ln σ b) ln ($\dot{\varepsilon}$) against σ c) ln ($\dot{\varepsilon}$) against ln (sinh (α σ_{sat})) d) ln (sinh (α σ_{sat})) against 1000/T(1/K) for VG.

Figure 4

See image above for figure legend

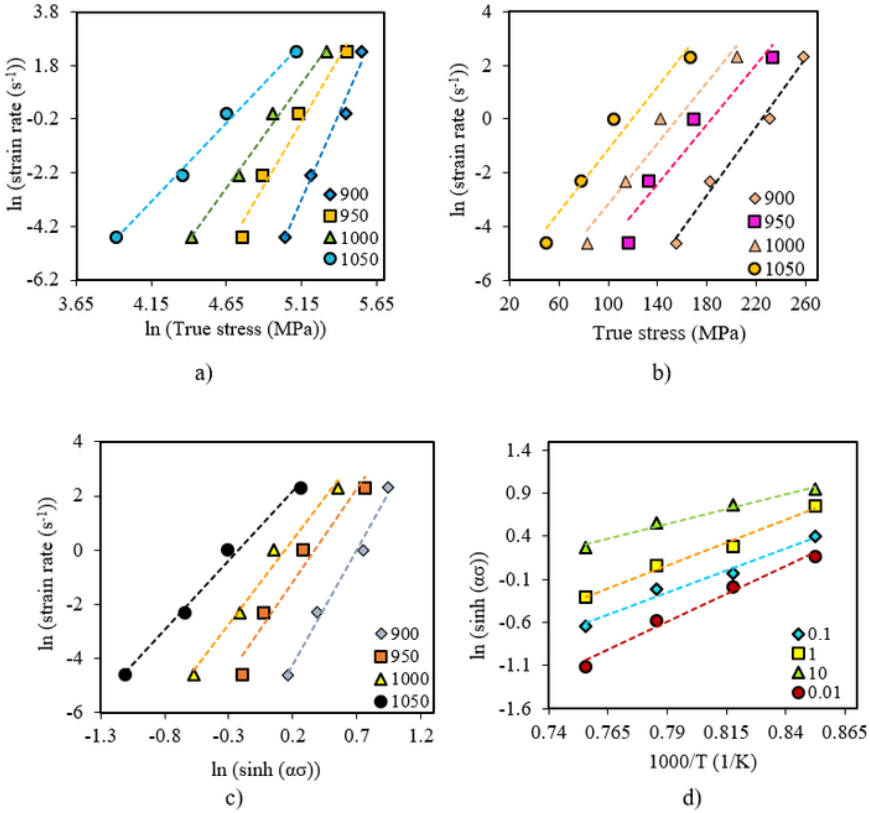

Fig. 5 Plots of a) ln ($\dot{\varepsilon}$) against ln σ b) ln ($\dot{\varepsilon}$) against σ c) ln ($\dot{\varepsilon}$) against ln (sinh (α σ_{sat})) d) ln (sinh (α σ_{sat})) against 1000/T(1/K) for CE

Figure 5

See image above for figure legend

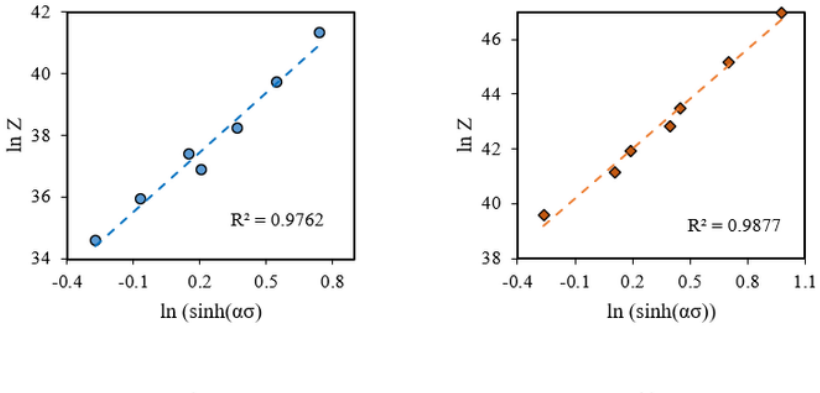

Fig. 6 The relationship between Ln Z against ln (sinh (ασ)) for a) VG and b) CE

Figure 6

See image above for figure legend

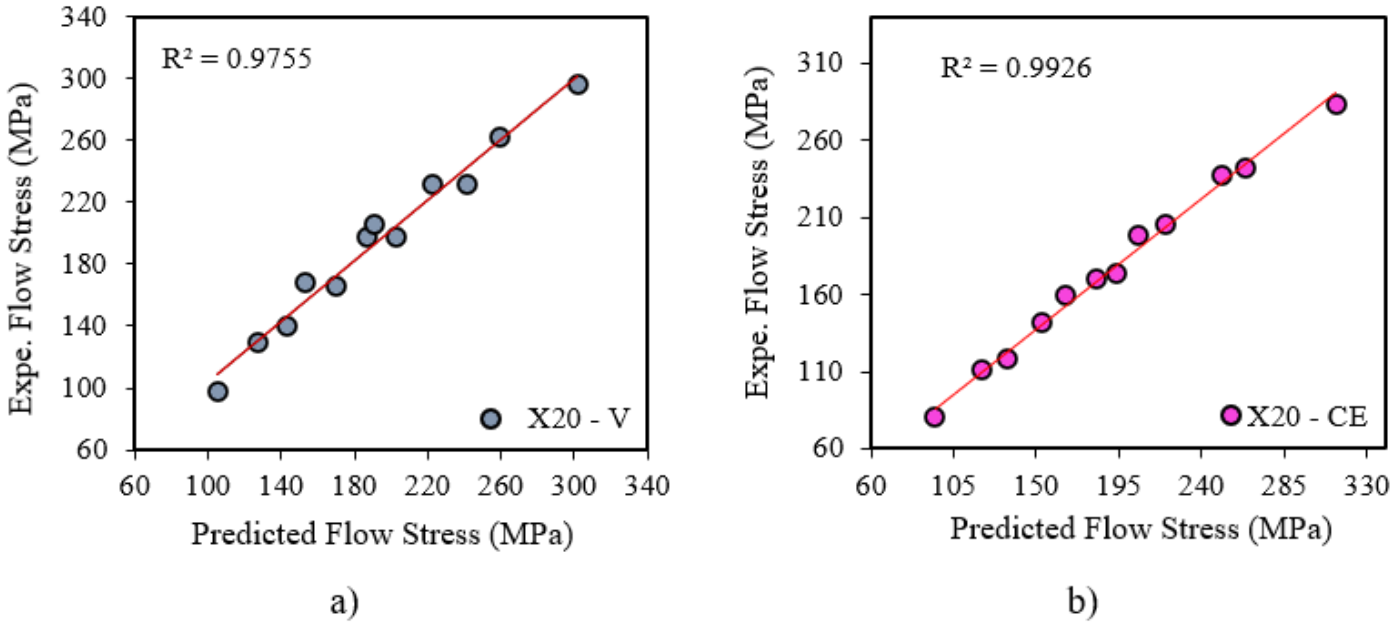

Figure 7

Comparison of experimental and predicted flow stress for a) VG b) CE